MONTHLY
WEATHER
REVIEW

VOLUME 93, NUMBER 7

JULY 1965

NUMERICAL INTEGRATION OF THE PRIMITIVE EQUATIONS ON A SPHERICAL GRID

YOSHIO KURIHARA [1]

Geophysical Fluid Dynamics Laboratory, U.S. Weather Bureau, Washington, D.C.

ABSTRACT

A new spherical grid system whose grid density on the globe is almost homogeneous is proposed. The elementary rules of finite differencing on the grid system are defined so that a desirable condition for numerical area integration is satisfied.

The integrations of primitive equations for a barotropic atmosphere with free surface are made. The patterns of initial fields are the same as Phillips used in 1959 for a test of his map projection system and computation schemes. Ten test runs are performed for a period of 16 days. Three of these are without viscosity and integrated with different time integration schemes. Four runs include the effect of non-linear viscosity with different coefficients, and the remaining three are computed with different amounts of linear viscosity. A noticeable distortion of the flow pattern does not occur in an early period in any run. Analyses of the results suggest that the damping of high frequency oscillation of both long and short wavelengths can be achieved by an iterative time integration scheme, e.g., the modified Euler-backward iteration method, with little effect on the prediction of a trend of the meteorological wave. Either the non-linear or the linear viscosity can be used to suppress a growth of short waves of both low and high frequency modes, if the optimum amount of viscosity for that purpose does not exceed the amount representing the actual diffusion process in the atmosphere. Analyses are also made concerning the effects caused by different specifications of the parameter in the viscosity term in the equations.

1. INTRODUCTION

In an application of grid methods to a meteorological problem, which requires a treatment on a global scale and also a time integration for a long period, we assume that two conditions are desirable. One is a homogeneous density of grid points on the globe. The other is the integral condition, i.e., that numerical integration of the difference analog of a quantity must correspond to the integral of its continuous form. Smagorinsky [10] considered this condition for establishing suitable computational boundary conditions which were required by the finite-difference system he used for a closed region. In this paper, however, the integral condition is used in the definition of the computational form of the flux divergence of a quantity. Namely, the estimation of flux divergence is related to an approximation of Gauss' theorem applied to an area element centered at a grid point. As a result, looseness at boundaries is avoided and the finite-difference sum of a quantity is exactly preserved.[2]

We often place a net of points on a projection of a spherical surface. In this case, we can consider that it is a projection of grid points originally fixed on the globe. Hereafter, we shall call the latter the original grid points.

A square mesh on a stereographic projection of one hemisphere satisfies approximately the requirement of homogeneous density of the original grid. A space increment on the earth increases from the equator to the pole by a factor of two. It is possible to establish a finite difference scheme so that the integral condition holds with respect to a quantity of the flux divergence type. Therefore, assuming lateral boundary conditions, we can

---

[1] On leave from the Meteorological Research Institute, Tokyo, Japan.

[2] Recently, Bryan (1965, personal communication) has suggested an approximation form of Gauss' theorem for a volume element bounded by surfaces of any shape. If his form is applied to a conservation equation, not only the finite-difference sum of the quantity but also its variance is preserved except for truncation due to time differencing. Accordingly, it is possible to formulate the so-called energy conserving schemes for the present spherical grid system.

apply this square mesh for a closed domain. It seems possible to treat a global scale problem by using two stereographic maps. In this case, a square mesh on each map has some extra points at the outside of the equator. Each of these points has a corresponding position within the equator on the other map. But the corresponding position does not always coincide with a point on the other map. Consequently a kind of interpolation is necessary for connecting the two maps. It is from this circumstance that a difficult problem arises. Namely, the scheme of interpolation, together with those of finite differencing and of area integration for an overlapping region, has to be determined so as to satisfy the integral condition. These schemes cannot be independent of each other. Even if we could formulate them, they might be too complicated to be practical. If we adopt a square mesh on a Mercator projection, we can easily extend a domain of integration without violating the integral condition. However, in this case, the change in density of the original grid is too large. A space increment is infinitesimally small at very high latitudes and the grid cannot reach the pole.

Phillips [5] proposed to use a Mercator map for low latitudes and stereographic projections for high latitudes and connect them at middle latitudes by overlapping grids. In his test system the distance between original grid points changes only by the factor of 1.4. Phillips [6, 7] used this map projection system in a numerical integration of primitive equations on a hemisphere. The integration was successfully performed for a barotropic divergent model for two or three days. A development of a discontinuity in the flow pattern in the overlapping region could be avoided with an interpolation scheme which was determined carefully. Also, an alternating uncentered-centered difference scheme in time derivative could not only eliminate the computational mode but also make a selective damping of short waves. The integral condition on this map system has not yet been discussed.

One way to make the density of the original grid nearly homogeneous is to change longitudinal and latitudinal increments at high latitudes as suggested by Richardson [8]. His plan was equivalent to using square meshes with variable size on a Mercator map. Kuo and Nordö [3] used this kind of grid system for integration of four-level prognostic equations over a hemisphere. An increment on the map was doubled at 60° latitude and doubled again at two higher latitudes. In their case, a certain computational instability, which was apparently connected with a change of mesh size, developed at the end of the fifth day.

A spherical grid system, in which a meridional increment is fixed and a zonal distance alone is doubled at higher latitudes, has been used by Gates and Riegel [1, 2] in the integration of simple atmospheric models. The results show that an abrupt change of zonal increment should not be made in the region of large tendency of stream function. Otherwise, a tearing of the stream function will be produced. Therefore, the doubling of the increment can be done only at high latitude. Because of this, the change of grid density becomes large. They also pointed out the importance of the integral condition.

Based upon the previously used grid systems described briefly above we propose a new grid method. The purposes of this study are as follows: (1) to establish a new spherical grid system and set up the elementary rules of finite differencing on the system, (2) to test the usefulness of the new grid system and the computation schemes by integrations of primitive equations for a barotropic model with a free surface, (3) to investigate the ways to suppress a high frequency oscillation as well as a growth of short waves in the results, and (4) to analyze the effects of the different types and the different amounts of viscosity.

2. A SPHERICAL GRID SYSTEM

In this section, we describe the new grid system. First, we put $N+1$ grid points at equal intervals along the meridian of 0° longitude from the north pole to the equator. We use an index (i, j) to identify a grid point on the earth. The grid points defined above are denoted by $(1, 1)$, $(1, 2)$, ... , $(1, N+1)$ respectively from the north pole toward the equator. We shall refer to the latitude circle which passes through the grid point $(1, j)$ as the jth latitude. The $(N+1)$th latitude coincides with the equator. Then, we place on each jth latitude, from $j=2$ to $j=N+1$, equally spaced $4\times(j-1)$ grid points, one of which is $(1, j)$. An index i increases in the eastward direction up to $4j-4$. In this way, the positions of grid points in the Northern Hemisphere are determined. Those in the Southern Hemisphere are symmetric to those in the Northern Hemisphere with respect to the equator. We call the system of all grid points thus located System 1 for the resolution N. Figure 1 is a schematic illustration of System 1 for the Northern Hemisphere and for a longitudinal range, $\lambda=0°$ through 90° E. The structures for the other three quarters are the same as in figure 1. The number of grid points on the entire surface for the N-resolution is $4N^2+2$.

The latitude and the longitude of a point $A(i, j)$, $j\neq 1$, on the Northern Hemisphere are as follows,

$$\theta_j=\frac{\pi}{2}\left(1-\frac{j-1}{N}\right)$$

$$\lambda_{i,j}=\frac{\pi}{2}\cdot\frac{i-1}{j-1} \tag{2.1}$$

Hence, we can define the increments in latitude and longitude, $\Delta\theta$ and $\Delta\lambda_j$, respectively,

$$\Delta\theta=\frac{\pi}{2}\frac{1}{N}$$

$$\Delta\lambda_j=\frac{\pi}{2}\cdot\frac{1}{j-1} \tag{2.2}$$

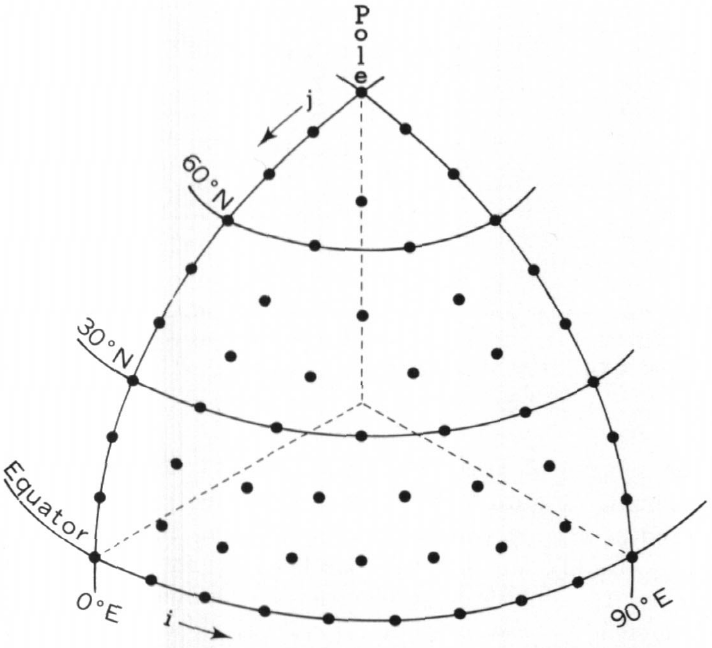

FIGURE 1.—Schematic illustration of System 1 for a quarter of the Northern Hemisphere.

The meridional and zonal increments on the earth are $a\Delta\theta$ and $a\cos\theta_j\ \Delta\lambda_j$ where a is the radius of the earth. The ratio of the latter to the former is unity if $j=N+1$. It is between 1 and $\pi/2$ for other j's; e.g., $3\sqrt{3}/4$ for $\theta_j=30°$, $\sqrt{2}$ for $\theta_j=45°$, 3/2 for $\theta_j=60°$, and $\pi/2$ for $\theta_j=90°$. The network of grid points is, therefore, slightly elongated in the zonal direction. However, for a given N, the meridional increment is fixed and the latitudinal change of zonal increment is gradual and varies by a factor of only $\pi/2$. Accordingly, the degree of homogeneity of grid density is very high in this new system as compared with other spherical grid systems used so far. Table 1 shows the increments at the equator, a middle latitude, and the pole for $N=20$. The corresponding values in the case of a square mesh on a stereographic map are also listed. (In this case, N means the number of equal subdivisions between the pole and the equator on the map.) The necessary number of grid points to cover the entire Northern Hemisphere including the equator for various N values on the new grid system and on the stereographic map are shown in table 2.

TABLE 1.—*The space increments at the equator, a middle latitude, and the pole. The values for* N=*20 are shown for the new spherical grid system and a square mesh on a stereographic map*

	New spherical grid $(a\Delta\theta)\times(a\cos\theta_j\ \Delta\lambda_j)$	Square mesh on stereographic map $\Delta x\times\Delta y$ (on the earth)
	km. km.	km. km.
Equator	500×500	319×319
45°	500×707	544×544
Pole	500×785	637×637

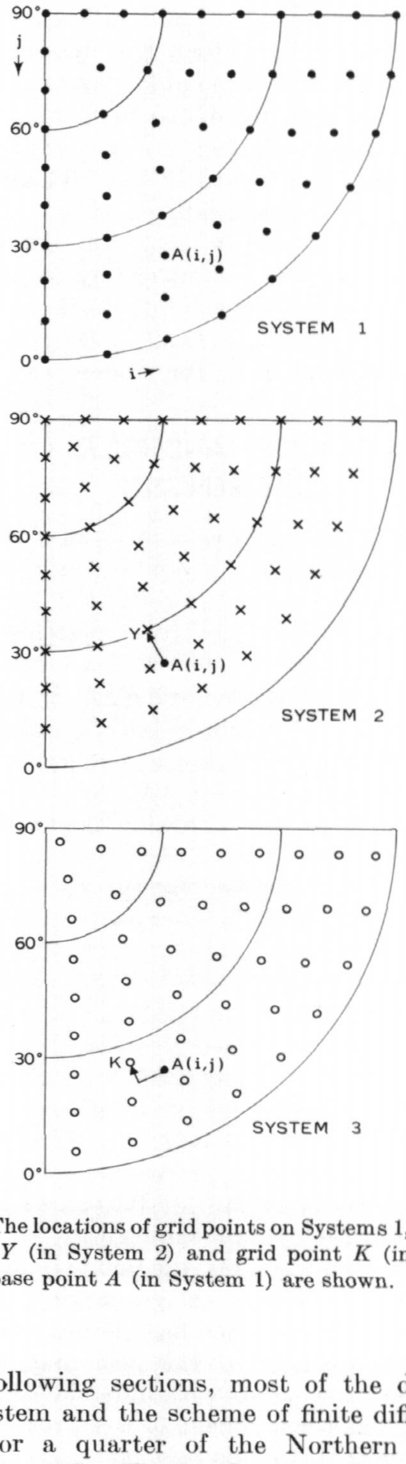

FIGURE 2.—The locations of grid points on Systems 1, 2, and 3. The grid point Y (in System 2) and grid point K (in System 3) for the given base point A (in System 1) are shown.

In the following sections, most of the description of the grid system and the scheme of finite differencing will be made for a quarter of the Northern Hemisphere, from $\lambda=0°$ to 90°. The results are to be applied to the other quarters and also to the Southern Hemisphere.

TABLE 2.—*The number of grid points necessary to cover the Northern Hemisphere including the Equator.* N *is the resolution*

N	New spherical grid	Square mesh on stereographic map
5	61	81
10	221	317
20	841	1257
40	3281	5025

For writing up a scheme of finite differencing, it is very convenient to define two other grid systems. Figure 2 shows the locations of grid points in Systems 1, 2, and 3, respectively. Let a point $A(i, j)$ in System 1 be a base point. We construct System 2 by shifting each grid point of System 1 northward by $\Delta\theta$. Therefore, a base point $A(i, j)$ has the corresponding grid point Y in System 2, at $\theta=\theta_j+\Delta\theta=\theta_{j-1}$ and $\lambda=\lambda_{i,j}$. On the other hand, moving a grid point $A(i, j)$ westward by $\Delta\lambda_j/2$ then northward by $\Delta\theta/2$ gives a corresponding position K at $\theta=\theta_j+(\Delta\theta/2)=\theta_{j-½}$ and $\lambda=\lambda_{i,j}-(\Delta\lambda_j/2)$. By relocating each grid point in System 1 in the above way, we obtain System 3.

3. INTERPOLATION AND RULES OF FINITE DIFFERENCING

Let us assume that the distribution of a certain quantity is given discretely for grid points of System 1. We have to estimate the values of System 2 and System 3. Figure 3 is a composite of the three systems; the points A, B, C, and D are on System 1, the points Y and Z are on System 2, and the points K, L, P, Q, R, and M belong to System 3. The grid value of a quantity, say X, will be denoted by a subscript which indicates a name or an index of the point, e.g., X_A or $X_{i,j}$. Then, X_Y is to be evaluated by the following linear interpolation formula,

$$\frac{X_Y-X_D}{X_C-X_D}=\frac{\lambda_Y-\lambda_D}{\lambda_C-\lambda_D} \tag{3.1}$$

where $\lambda_Y=\lambda_A$. $A(i,j)$ is the base point. With the use of (2.1), (3.1) is rewritten, for a given j where $j\geq 3$.

$$X_Y=\begin{cases}\dfrac{i-1}{j-1}\,X_{i-1,\,j-1}+\dfrac{j-i}{j-1}\,X_{i,\,j-1} & \text{for } j\geq i\geq 1\\[2ex] \dfrac{j-2}{j-1}\,X_{0,\,j-1}+\dfrac{1}{j-1}\,X_{1,\,j-1} & \text{for } i=0\end{cases}$$

In general, $A(0, j)=A(4j-4, j)$. We can evaluate X_Z for the base point $B(i-1, j)$ in a similar way.

For the base point $A(i, 2)$, the point Y coincides with the north pole. If X is a scalar quantity, X_Y does not depend on the index i of the base point. On the other hand, a vector quantity at the pole may be observed differently from base points with different i-indices. Accordingly, if X is a component of a vector quantity, we have to assume that, for the base point $A(i, 2)$, $X_Y=X_{i,1}$ $(i=1, 2, 3, 4)$. We shall discuss the pole value, $X_{i,1}$, in the next section.

The interpolation formula (3.2) yields X_K,

$$X_K=\tfrac{1}{4}(X_A+X_B+X_Y+X_Z) \tag{3.2}$$

The values at the points L, P, Q, R, and M, the base points for which are $(i+1, j)$, $(i, j+1)$, $(i+1, j+1)$, $(i+2, j+1)$ and $(i-1, j+1)$ respectively, can be estimated by the same principle.

Our next problem is to establish the rules for finite differencing. As this problem is closely connected with the scheme of area integration, we first define an area element. Figure 4 shows an area element, which is centered at $A(i, j)$ and surrounded by the two meridians, $\lambda_{i,j}\pm(\Delta\lambda_j/2)$, and the two parallels, $\theta_j\pm(\Delta\theta/2)$. For the point $A(1, 1)$, the area element is the small polar cap bounded by the latitude $(\pi-\Delta\theta)/2$. The area of an element is exactly given by (3.3),

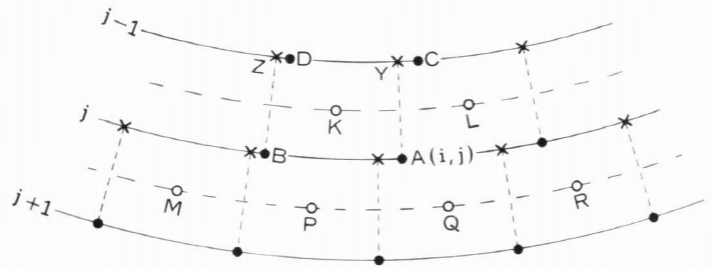

FIGURE 3.—Composite of the three grid systems. Grid points in Systems 1, 2, and 3 are indicated by black circles, cross marks, and open circles, respectively.

$$\Delta S_j=\begin{cases}2a^2\Delta\lambda_j\cos\theta_j\sin\dfrac{\Delta\theta}{2} & \text{for } j\geq 2\\[2ex] 2\pi a^2\left(1-\cos\dfrac{\Delta\theta}{2}\right) & \text{for } j=1\end{cases} \tag{3.3}$$

We make the rule that the total area integration of the quantity X is to be computed by the right-hand side of (3.4),

$$\iint XdS\approx\sum_j\left(\sum_i X_{i,j}\,\Delta S_j\right) \tag{3.4}$$

where the summations are taken for all grid points of System 1. The quantity in parentheses in (3.4) shows an area integral for the jth zonal ring which is formed by the two latitudes $\theta_j\pm(\Delta\theta/2)$. If $X=X_{i,j}=1$, (3.4) gives the exact area of a spherical surface, i.e., $4\pi a^2$.

It is convenient to define the side values of X. These are the integrated means of X along each of the north, south, east, and west sides of an area element. In case of the small north polar cap, we have only the south side value. The line integrals along the north and the south sides are evaluated by linearly interpolating between grid values in System 3. For example, for the base point $A(i, j)$ in figure 3, the north side value is as follows,

$$\frac{1}{\Delta\lambda_j}\int_{\lambda_{i,j}-(\Delta\lambda_j/2)}^{\lambda_{i,j}+(\Delta\lambda_j/2)} X\left(\lambda,\,\theta_j+\frac{\Delta\theta}{2}\right)d\lambda\approx\frac{X_K+X_L}{2}\equiv(X_N)_{i,j} \tag{3.5}$$

The south side value, except for the case $i=1$, is given by

$$\frac{1}{\Delta\lambda_j}\int_{\lambda_{i,j}-(\Delta\lambda_j/2)}^{\lambda_{i,j}+(\Delta\lambda_j/2)} X\left(\lambda,\,\theta_j-\frac{\Delta\theta}{2}\right)d\lambda$$

$$\approx\frac{1}{\Delta\lambda_j}\left\{\frac{X_k+X_Q}{2}\,(\lambda_Q-\lambda_k)+\frac{X_Q+X_l}{2}\,(\lambda_l-\lambda_Q)\right\}$$

$$\equiv(X_S)_{i,j}\qquad\text{for } 2\leq i\leq j-1 \tag{3.6}$$

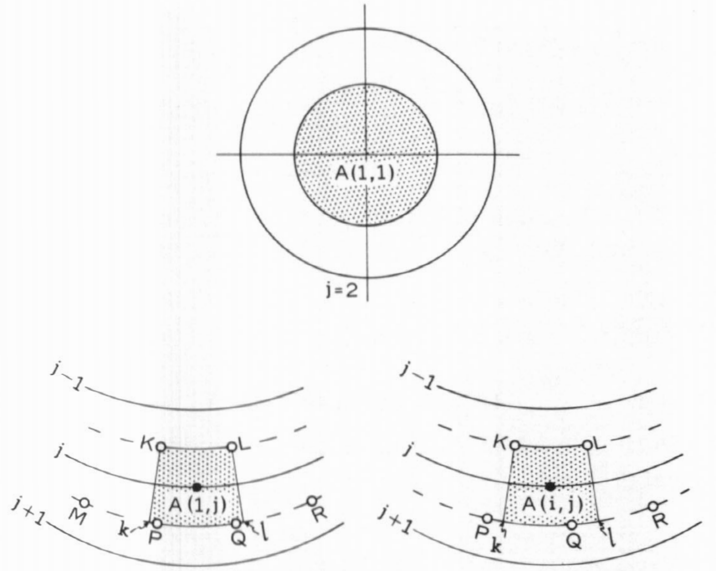

FIGURE 4.—Area elements, centered at $A(1,1)$, $A(1,j)$, and $A(i,j)$ respectively, are shown by shading. k and l are southwestern and southeastern corners of an area element.

Here, the point k between P and Q and the point l between Q and R are the southwestern and southeastern corners of an area element, respectively. In the case $i=1$, when k takes a position between M and P, we use (3.7) instead of (3.6),

$$\frac{1}{\Delta\lambda_j}\left\{\frac{X_k+X_P}{2}(\lambda_p-\lambda_k)+\frac{X_p+X_Q}{2}(\lambda_Q-\lambda_P)+\frac{X_Q+X_l}{2}(\lambda_l-\lambda_Q)\right\}\equiv(X_S)_{1,j} \quad (3.7)$$

X_k and X_l in (3.6) and (3.7) are linearly interpolated values. Namely, for a specified base point $A(i,j)$,

$$X_k=\begin{cases}\dfrac{j-i+0.5}{j-1}X_P+\left(1-\dfrac{j-i+0.5}{j-1}\right)X_Q & \text{if } j\geq 3 \text{ and } j-1\geq i\geq 2\\ \dfrac{0.5}{j-1}X_M+\left(1-\dfrac{0.5}{j-1}\right)X_P, & \text{if } j\geq 2 \text{ and } i=1\end{cases}$$

$$X_l=\left(1-\frac{i-0.5}{j-1}\right)X_Q+\frac{i-0.5}{j-1}X_R, \quad \text{if } j\geq 2 \text{ and } j-1\geq 1i\geq.$$

Then, $(X_S)_{i,j}$ takes the following form,

$$(X_S)_{i,j}=\frac{(j-i+0.5)^2}{2j(j-1)}X_P+\left\{1-\frac{(j-i+0.5)^2+(i-0.5)^2}{2j(j-1)}\right\}X_Q+\frac{(i-0.5)^2}{2j(j-1)}X_R, \quad \text{if } j\geq 3 \text{ and } j-1\geq i\geq 2 \quad (3.8)$$

$$(X_S)_{1,j}=\frac{1}{8j(j-1)}(X_M+X_R)+\left(\frac{1}{2}-\frac{1}{8j(j-1)}\right)(X_P+X_Q) \quad \text{if } j\geq 2 \text{ and } i=1 \quad (3.9)$$

$(X_S)_{i,j}$ is a weighted mean of X_M, X_P, X_Q, and X_R. In computer programming, it is practical to calculate these weights at the beginning and keep them in storage. It should be noted that $(X_N)_{i,j+1}$ and $(X_S)_{i,j}$ are integrated means along the same latitude, i.e., $\theta_{j+½}=\theta_j-(\Delta\theta/2)$, although the longitudinal ranges of integration are different. Therefore, the following relation is satisfied,

$$\sum_{i=1}^{4j-4}(X_S)_{i,j}\,a\cos\theta_{j+½}\Delta\lambda_j=\sum_{i=1}^{4(j+1)-4}(X_N)_{i,j+1}\,a\cos\theta_{j+½}\Delta\lambda_{j+1} \quad (3.10)$$

If meridional transfer of a certain quantity is represented by X, (3.10) means that inflow of the quantity into the jth zonal ring across the southern boundary is equal to outflow from the $(j+1)$th zonal ring across the northern boundary.

The east and the west side values for the base point $A(i,j)$ are defined as follows,

$$\frac{1}{\Delta\theta}\int_{\theta_j-(\Delta\theta/2)}^{\theta_j+(\Delta\theta/2)}X\left(\lambda_{i,j}+\frac{\Delta\lambda_j}{2},\theta\right)d\theta\approx\frac{X_L+X_l}{2}\equiv(X_E)_{i,j} \quad (3.11)$$

$$\frac{1}{\Delta\theta}\int_{\theta_j-(\Delta\theta/2)}^{\theta_j+(\Delta\theta/2)}X\left(\lambda_{i,j}-\frac{\Delta\lambda_j}{2},\theta\right)d\theta\approx\frac{X_K+X_k}{2}\equiv(X_W)_{i,j} \quad (3.12)$$

The requirement

$$(X_E)_{i,j}=(X_W)_{i+1,j} \quad (3.13)$$

is satisfied by the above definitions.

The elementary rules of finite differencing on the new grid system are written below. The subscript i, j which is attached to the side values in (3.5), (3.6), (3.7), (3.11), and (3.12) will be omitted hereafter.

FLUX DIVERGENCE

We define the zonal component of the flux divergence of a quantity, say X, by (3.14),

$$\left(\frac{\partial uX}{a\cos\theta\partial\lambda}\right)_{i,j}\approx\frac{1}{a\cos\theta_j\Delta\lambda_j}\frac{\Delta\theta}{2\sin(\Delta\theta/2)}(u_EX_E-u_WX_W) \quad \text{for } j\geq 2 \quad (3.14)$$

where u is the eastward component of the wind. The meridional component of the flux divergence is obtained by (3.15)

$$\left(\frac{\partial vX\cos\theta}{a\cos\theta\partial\theta}\right)_{i,j}\approx\frac{1}{a\cos\theta_j\Delta\theta}\frac{\Delta\theta}{2\sin(\Delta\theta/2)}\times\{(vX)_N\cos\theta_{j-½}-(vX)_S\cos\theta_{j+½}\} \quad \text{for } j\geq 2 \quad (3.15)$$

where v is the northward component of the wind.

The above definitions of flux divergence rest on the following basis. If we multiply the sum of (3.14) and (3.15) by (3.3), we have

$$\left(\frac{\partial uX}{a\cos\theta\partial\lambda}+\frac{\partial vX\cos\theta}{a\cos\theta\partial\theta}\right)_{i,j}\Delta S_j=(\nabla\cdot\mathbf{V}X)_{i,j}\cdot\Delta S_j\approx u_E X_E\cdot a\Delta\theta$$
$$-u_W X_W\cdot a\Delta\theta+(vX)_N\cdot a\Delta\lambda_j\cos\theta_{j-\frac{1}{2}}$$
$$-(vX)_S\cdot a\Delta\lambda_j\cos\theta_{j+\frac{1}{2}}\qquad\text{for } j\geq 2\quad(3.16)$$

In (3.16), $a\Delta\theta$ is the length of the east and the west sides, $a\Delta\lambda_j\cos\theta_{j-\frac{1}{2}}$ is that of the north side, and $a\Delta\lambda_j\cos\theta_{j+\frac{1}{2}}$ is that of the south side. Consequently, the relation (3.16) is equivalent to Gauss' theorem and the integral condition can be satisfied locally at each area element. Note that a meridional transfer is estimated not by $v_N X_N$ or $v_S X_S$ but by $(vX)_N$ or $(vX)_S$. This procedure is necessary in order that the important condition (3.10) with X replaced by vX is satisfied. The idea of an appropriate use of an integrated mean value along a side of an area element seems to be applicable generally to a grid system with a variable increment size.

To estimate the flux divergence for the small polar cap, we use (3.17),

$$\left(\frac{\partial uX}{a\cos\theta\partial\lambda}+\frac{\partial vX\cos\theta}{a\cos\theta\partial\theta}\right)_{1,1}\approx-\frac{\sin\frac{\Delta\theta}{2}}{4a\left(1-\cos\frac{\Delta\theta}{2}\right)}\sum_{i=1}^{4}((vX)_N)_{i,2}\qquad(3.17)$$

If (3.17) is multiplied by (3.3) for $j=1$, the right-hand side gives a line integral of outward flux across the boundary of the polar cap.

DIVERGENCE OF WIND

Putting $X=1$ in the sum of (3.14) and (3.15), we get a formula to calculate the divergence of wind

$$\left(\frac{\partial u}{a\cos\theta\partial\lambda}+\frac{\partial v\cos\theta}{a\cos\theta\partial\theta}\right)_{i,j}=(\nabla\cdot\mathbf{V})_{i,j}\approx\frac{1}{a\cos\theta_j\Delta\lambda_j}\frac{1}{2\sin(\Delta\theta/2)}$$
$$\{\Delta\theta(u_E-u_W)+\Delta\lambda_j(v_N\cos\theta_{j-\frac{1}{2}}-v_S\cos\theta_{j+\frac{1}{2}})\}\qquad\text{for } j\geq 2\qquad(3.18)$$

The formula for $j=1$ can be obtained by putting $X=1$ in (3.17). We can, therefore, estimate the vertical component of the wind at each grid point of System 1 with the continuity equation and a proper boundary condition.

HORIZONTAL ADVECTION

By subtracting (3.18) multiplied by $(X_E+X_W)/2$ from the sum of (3.14) and (3.15), we get the formula for horizontal advection. This process corresponds to $\nabla\cdot(\mathbf{V}X)-X\nabla\cdot\mathbf{V}=\mathbf{V}\cdot\nabla X$. The results written separately for each component are

$$\left(u\frac{\partial X}{a\cos\theta\partial\lambda}\right)_{i,j}\approx\frac{u_E+u_W}{2}\frac{1}{a\cos\theta_j\Delta\lambda_j}\frac{\Delta\theta}{2\sin(\Delta\theta/2)}(X_E-X_W)\qquad(3.19)$$

$$\left(v\frac{\partial X}{a\partial\theta}\right)_{i,j}\approx\frac{1}{2a\cos\theta_j\sin(\Delta\theta/2)}\left\{(vX)_N\cos\theta_{j-\frac{1}{2}}\right.$$
$$\left.-(vX)_S\cos\theta_{j+\frac{1}{2}}-\frac{X_E+X_W}{2}(v_N\cos\theta_{j-\frac{1}{2}}-v_S\cos\theta_{j+\frac{1}{2}})\right\}\qquad(3.20)$$

If X is a function of latitude only, $(vX)_N=v_N X_N$, $(vX)_S=v_S X_S$, and $X_E=X_W=(X_N+X_S)/2$. Then, (3.20) becomes

$$\left(v\frac{\partial X}{a\partial\theta}\right)_{i,j}\approx\frac{v_N\cos\theta_{j-\frac{1}{2}}+v_S\cos\theta_{j+\frac{1}{2}}}{\cos\theta_{j-\frac{1}{2}}+\cos\theta_{j+\frac{1}{2}}}\frac{\cos(\Delta\theta/2)}{2a\sin(\Delta\theta/2)}(X_N-X_S)$$

HORIZONTAL GRADIENT

Putting $u=1$ in (3.19), we get a formula to estimate zonal gradient,

$$\left(\frac{\partial X}{a\cos\theta\partial\lambda}\right)_{i,j}\approx\frac{1}{a\cos\theta_j\Delta\lambda_j}\frac{\Delta\theta}{2\sin(\Delta\theta/2)}(X_E-X_W)\qquad(3.21)$$

If we make the definition

$$\left(\frac{\partial X}{\partial\lambda}\right)_{i,j}=\left(\frac{\partial X}{a\cos\theta\partial\lambda}\right)_{i,j}\times a\frac{\cos\theta_{j-\frac{1}{2}}+\cos\theta_{j+\frac{1}{2}}}{2}$$

it follows that

$$\left(\frac{\partial X}{\partial\lambda}\right)_{i,j}\approx\frac{1}{\Delta\lambda_j}\frac{\Delta\theta\cos(\Delta\theta/2)}{2\sin(\Delta\theta/2)}(X_E-X_W)\qquad(3.22)$$

We can deduce a formula for meridional gradient from (3.20) by putting $v=1$ and assuming $X_E+X_W=X_N+X_S$. It takes the form

$$\left(\frac{\partial X}{a\partial\theta}\right)_{i,j}\approx\frac{1}{a\Delta\theta}\frac{\Delta\theta\cos(\Delta\theta/2)}{2\sin(\Delta\theta/2)}(X_N-X_S)\qquad(3.23)$$

In the rules of finite differencing, we often have such factors as $\Delta\theta/(2\sin(\Delta\theta/2))$ or $(\Delta\theta\cos(\Delta\theta/2)/(2\sin(\Delta\theta/2))$. These are almost unity and approach it with increasing N or decreasing $\Delta\theta$. When $N=10$, these factors are 1.001 and 0.998, respectively.

In establishing the schemes of finite differencing, we have examined many different schemes. Those presented in this paper are the best ones in the sense that they yield the most stable integration of the equations in the next section. The study by Shuman [9] was very useful in many respects. It may be worth saying that the key point of our work was not to use the grid values of System 1 but to use those of System 3 for estimating the tendencies at grid points of System 1. All the test computations which used the grid values of System 1 directly and did not have terms of viscosity became computationally unstable within a short time. This is probably due to a rapid growth of the shortest resolvable wave. The grid values of System 3 are obtained by (3.2). In this process, the waves of the scale of two space increments are filtered out. Therefore, if System 3 is used in tendency calculations, a direct feedback of the influence of the short waves to System 1 can be avoided. As for an interpolation scheme to compute the grid values of System 3, we examined several forms and reached the conclusion that we could continue the test integration most satisfactorily using the simplest formula (3.2).

4. EQUATIONS FOR A NUMERICAL TEST OF THE NEW SPHERICAL GRID

We tested the new spherical grid system and the rules of finite differencing by the integration of primitive equations. The atmospheric model and the initial fields we adopted are the same as those used by Phillips [7] in a test of the grid system which he proposed. He made an analysis of the behavior of this numerical model and, accordingly, we can utilize it. In the test computations, we also attempted to overcome difficulties associated with high-frequency oscillations and the growth of short waves.

It is known that, from the viewpoint of the budget of absolute angular momentum, the Coriolis term and the metric term in the longitudinal component of the equation of motion are related to the flux divergence of the angular momentum due to the rotation of the earth and that of the relative angular momentum, respectively. In this study, these terms in the difference form of the equation of motion can be combined with the terms in the difference form of the continuity equation to form the flux divergences which correspond to the above interpretation. Consequently, the conservation of absolute angular momentum is highly guaranteed. The prognostic equations are derived as follows.

Lagrange's form of the equation of motion for an inviscid fluid on a rotating sphere is written in the spherical coordinate system (λ, θ, r)

$$\frac{d}{dt}\left(\frac{\partial L}{\partial \dot{q}}\right)-\frac{\partial L}{\partial q}=0, \qquad q=\lambda, \theta, r \tag{4.1}$$

where

$$\frac{d}{dt}=\frac{\partial}{\partial t}+\dot{\lambda}\frac{\partial}{\partial \lambda}+\dot{\theta}\frac{\partial}{\partial \theta}+\dot{r}\frac{\partial}{\partial r}$$

r is the radial distance from the center of the sphere and L is the Lagrangian function. L is given by

$$L=\tfrac{1}{2}\{(r\cos\theta\dot{\lambda}+r\cos\theta\Omega)^2+(r\dot{\theta})^2+\dot{r}^2\}-\Phi \tag{4.2}$$

where Ω is the angular velocity of the sphere and Φ, the potential of gravity force plus pressure gradient force. We can redefine the coordinate system so that the meridional component of centrifugal force cancels that of the gravity force and the coordinate r is taken along the true vertical. Furthermore, we assume the hydrostatic relation, which requires the elimination of some terms in the equations for energetical consistency. Then, converting to the (λ, θ, p) coordinate system, where p is pressure, we obtain the following equations,

$$\frac{\partial}{\partial t}(r\cos\theta\,\dot{\lambda})+\dot{\lambda}\frac{\partial}{\partial \lambda}(r\cos\theta\,\dot{\lambda})+\frac{\dot{\theta}}{\cos\theta}\frac{\partial}{\partial \theta}(r\cos^2\theta\,\dot{\lambda})$$
$$+\dot{p}\frac{\partial}{\partial p}(r\cos\theta\,\dot{\lambda})+\frac{r\dot{\theta}\Omega}{\cos\theta}\frac{\partial}{\partial \theta}(\cos^2\theta)+\frac{\partial \phi}{r\cos\theta\partial\lambda}=0 \tag{4.3}$$

$$\frac{\partial}{\partial t}(r\dot{\theta})+\dot{\lambda}\frac{\partial}{\partial \lambda}(r\dot{\theta})+\dot{\theta}\frac{\partial}{\partial \theta}(r\dot{\theta})+\dot{p}\frac{\partial}{\partial p}(r\dot{\theta})$$
$$-\frac{1}{2}r\dot{\lambda}^2\frac{\partial}{\partial \theta}(\cos^2\theta)-r\dot{\lambda}\Omega\frac{\partial}{\partial \theta}(\cos^2\theta)+\frac{\partial\phi}{r\partial\theta}=0 \tag{4.4}$$

where ϕ is the geopotential of an isobaric surface. Introducing $\dot{\lambda}=u/(r\cos\theta)$ and $\dot{\theta}=v/r$ into (4.3) and (4.4), and putting $r=a=$earth's mean radius, we obtain the equations for u and v, which are the conventional variables,

$$\frac{\partial u}{\partial t}=-u\frac{\partial u}{a\cos\theta\partial\lambda}-\frac{v}{\cos\theta}\frac{\partial u\cos\theta}{a\partial\theta}-\dot{p}\frac{\partial u}{\partial p}$$
$$-\frac{v\Omega}{\cos\theta}\frac{\partial\cos^2\theta}{\partial\theta}-\frac{\partial\phi}{a\cos\theta\partial\lambda} \tag{4.5}$$

$$\frac{\partial v}{\partial t}=-u\frac{\partial v}{a\cos\theta\partial\lambda}-v\frac{\partial v}{a\partial\theta}-\dot{p}\frac{\partial v}{\partial p}+\frac{u^2}{2a\cos^2\theta}\frac{\partial\cos^2\theta}{\partial\theta}$$
$$+\frac{u\Omega}{\cos\theta}\frac{\partial\cos^2\theta}{\partial\theta}-\frac{\partial\phi}{a\partial\theta} \tag{4.6}$$

In (4.5), the so-called metric term is included in the second term on the right-hand side and the Coriolis term is represented by the fourth term. They originate from the advection of the absolute angular momentum, i.e., the first term in (4.1). The source of the metric term and of the Coriolis term in (4.6), i.e., the fourth and fifth terms on the right-hand side respectively, is the second term in (4.1).

If the homogeneous atmosphere with a variable depth $z\ (=\phi/g)$ is assumed, the tendency of ϕ is given by (4.7),

$$\frac{\partial\phi}{\partial t}=-\frac{\partial\phi u}{a\cos\theta\partial\lambda}-\frac{\partial\phi v\cos\theta}{a\cos\theta\partial\theta}\equiv H \tag{4.7}$$

As the integral condition will be used in the estimation of flux divergence of ϕ in the difference form of (4.7), the finite-difference sum of ϕ will be preserved. The equations for $U=u\phi$ and $V=v\phi$ in the homogeneous atmosphere are derived from (4.5), (4.6), and (4.7),

$$\frac{\partial U}{\partial t}=-\frac{\partial(u\phi u)}{a\cos\theta\partial\lambda}-\frac{1}{\cos\theta}\frac{\partial(u\phi\cos\theta v\cos\theta)}{a\cos\theta\partial\theta}$$
$$-v\phi\Omega\frac{\partial(\cos^2\theta)}{\cos\theta\partial\theta}-\phi\frac{\partial\phi}{a\cos\theta\partial\lambda}\equiv G_\lambda \tag{4.8}$$

$$\frac{\partial V}{\partial t}=-\frac{\partial(v\phi u)}{a\cos\theta\partial\lambda}-\frac{\partial(v\phi v\cos\theta)}{a\cos\theta\partial\theta}+\frac{u^2\phi}{a}\frac{\partial(\cos^2\theta)}{2\cos^2\theta\partial\theta}$$
$$+u\phi\Omega\frac{\partial(\cos^2\theta)}{\cos\theta\partial\theta}-\phi\frac{\partial\phi}{a\partial\theta}\equiv G_\theta \tag{4.9}$$

A system of prognostic equations for the barotropic divergent model consists of (4.7), (4.8), and (4.9). From (4.7) and (4.8) we have the equation which is equivalent to (4.1),

$$\frac{\partial R}{\partial t}=-\frac{\partial Ru}{a\cos\theta\partial\lambda}-\frac{\partial Rv\cos\theta}{a\cos\theta\partial\theta}-\frac{\partial}{\partial\lambda}\left(\frac{\phi^2}{2}\right)$$

where R is the absolute angular momentum of an air column; $R=(u+a\Omega\cos\theta)a\phi\cos\theta$. As a similar manipulation is possible with respect to the following difference forms of (4.7) and (4.8), we can anticipate the conservation of the finite-difference sum of the absolute angular momentum.

In order to estimate G_λ and G_θ by the rules of finite differencing defined in the previous section, we have to evaluate u, v and ϕ in System 3. We can easily obtain these values from the System 1 values of u and v (obtained from U/ϕ and V/ϕ respectively) by using the interpolation formulae in section 3. The finite-difference forms of G_λ and G_θ for $j\geq 2$ are

$$\begin{aligned}(G_\lambda)_{i,j}\approx&-\alpha_1(u_E\phi_Eu_E-u_W\phi_Wu_W)\\&-\frac{2}{\cos\theta_{j-1/2}+\cos\theta_{j+1/2}}\alpha_2\times\\&\{(u\phi v)_N\cos^2\theta_{j-1/2}-(u\phi v)_S\cos^2\theta_{j+1/2}\}\\&+f_j\frac{(v\phi)_N\cos\theta_{j-1/2}+(v\phi)_S\cos\theta_{j+1/2}}{\cos\theta_{j-1/2}+\cos\theta_{j+1/2}}\\&-\alpha_1\frac{\phi_E+\phi_W}{2}(\phi_E-\phi_W)\end{aligned}\tag{4.10}$$

$$\begin{aligned}(G_\theta)_{i,j}\approx&-\alpha_1(v_E\phi_Eu_E-v_W\phi_Wu_W)\\&-\alpha_2\{(v\phi v)_N\cos\theta_{j-1/2}-(v\phi v)_S\cos\theta_{j+1/2}\}\\&-m_j\left(\frac{u_N+u_S}{2}\right)^2\frac{\phi_N+\phi_S}{2}-f_j\frac{u_N+u_S}{2}\frac{\phi_N+\phi_S}{2}\\&-\alpha_3\frac{\phi_E+\phi_W}{2}(\phi_N-\phi_S)\end{aligned}\tag{4.11}$$

where

$$\alpha_1=\frac{1}{a\cos\theta_j\Delta\lambda_j}\frac{\Delta\theta}{2\sin(\Delta\theta/2)}$$

$$\alpha_2=\frac{1}{a\cos\theta_j\Delta\theta}\frac{\Delta\theta}{2\sin(\Delta\theta/2)}$$

$$\alpha_3=\frac{1}{a\Delta\theta}\frac{\Delta\theta\cos(\Delta\theta/2)}{2\sin(\Delta\theta/2)}$$

$$\begin{aligned}f_j=&\frac{2a\Omega}{\cos\theta_{j-1/2}+\cos\theta_{j+1/2}}\alpha_3(\cos^2\theta_{j+1/2}-\cos^2\theta_{j-1/2})\\&=2\Omega\sin\theta_j\cos(\Delta\theta/2)\end{aligned}$$

$$m_j=\frac{1}{2}\left(\frac{2}{\cos\theta_{j-1/2}+\cos\theta_{j+1/2}}\right)^2\alpha_3(\cos^2\theta_{j+1/2}-\cos^2\theta_{j-1/2})=\frac{\tan\theta_j}{a}\tag{4.12}$$

For the factors $u^2\phi$ and $u\phi$ in (4.9), we have no rules of estimation. Several schemes, including weighting the north side and the south side values by $\cos\theta$, were tested. The most stable numerical integration was obtained with the use of the simple schemes as shown by the third and the fourth terms in (4.11). It may be interesting that f_j is equal to the area mean of the Coriolis parameter, i.e., $f_j=\int 2\Omega\sin\theta\, dS/\int dS$, where $\int dS=\Delta S_j$ is the area of an area element. The quantity m_j is equal to the area mean of $\tan\theta/a$, i.e., $m_j=\int(\tan\theta/a)dS/\int dS$. In (4.10) and (4.11), the north and the south side values of a quantity of the product type are weighted means of the products at grid points of System 3. For example, $(uv\phi)_N=(u_Kv_K\phi_K+u_Lv_L\phi_L)/2$. (See fig. 3.) The computation scheme of (4.7) is written

$$H_{i,j}\approx-\alpha_1(\phi_Eu_E-\phi_Wu_W)-\alpha_2\{(\phi v)_N\cos\theta_{j-1/2}-(\phi v)_S\cos\theta_{j+1/2}\}\qquad\text{for } j\geq 2\tag{4.13}$$

We use (3.17) to obtain a scheme for $j=1$.

$$H_{1,1}\approx\frac{\sin\frac{\Delta\theta}{2}}{4a\left(1-\cos\frac{\Delta\theta}{2}\right)}\sum_{i=1}^{4}((\phi v)_N)_{i,2}\tag{4.14}$$

Although we assumed a calm condition at the pole in our test, we should consider how to treat the wind at the pole in general. One scheme, which should be tested in the future, is described in the following. Figure 5 is

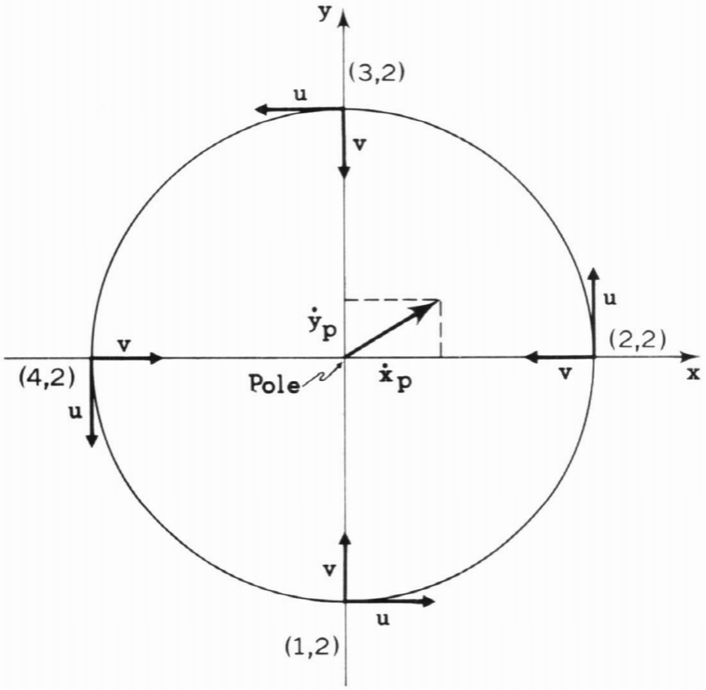

FIGURE 5.—Stereographic projection of a polar region. The corresponding index in System 1 is shown for each grid point surrounding the pole. $\dot{x}_p$ and $\dot{y}_p$ are components of the pole wind.

a stereographic projection of a polar region. The four grid points which have the index $j=2$ in System 1 are projected around the pole. Taking the map axis as shown in the figure, we can define the map velocity, $\dot{x}$ and $\dot{y}$. For example, $\dot{x}$ and $\dot{y}$ at the point to the right of the pole are proportional to $-v$ and u at the grid point (2, 2) of System 1. By using $\dot{x}$, and $\dot{y}$, and ϕ at the pole and the surrounding points, we can estimate the tendencies of $\dot{x}$ and $\dot{y}$ at the pole with the equations written in map coordinates. We denote $\dot{x}$ and $\dot{y}$ at the pole by $\dot{x}_p$ and $\dot{y}_p$. Then, if we see the wind at the pole from the grid point (1, 2) of System 1, we will observe $\dot{x}_p$ as an eastward component and $\dot{y}_p$ as a northward component. In this case the pole is considered to be the point (1, 1). While from the grid point (2, 2), $\dot{y}_p$ will be observed as an eastward component and $\dot{x}_p$ as a southward component. The pole is then taken as the point (2, 1). In this way, the following definition of the pole values can be made,

$$\begin{array}{ll} u_{1,1}=\dot{x}_p & v_{1,1}=\dot{y}_p \\ u_{2,1}=\dot{y}_p & v_{2,1}=-\dot{x}_p \\ u_{3,1}=-\dot{x}_p & v_{3,1}=-\dot{y}_p \\ u_{4,1}=-\dot{y}_p & v_{4,1}=\dot{x}_p \end{array}$$

As mentioned in section 3, these values are taken as u_Y and v_Y for the base point $A(i, 2)$. In the case of a scalar quantity, the pole value does not change with the index i. For example $\phi_{i,1}=\phi_p$ for $i=1$, 2, 3 and 4.

Smagorinsky (to be published) made a formulation of non-linear lateral diffusion which he assumed to represent an effect of motions of unresolvable scale. In some test computations, we add this kind of viscosity term to the tendency equations (4.8) and (4.9). These terms, denoted by F_λ and F_θ, take the form

$$F_\lambda=2(k_0 a\Delta\theta)^2\left\{\frac{\partial}{a\cos\theta\partial\lambda}(n\phi|D|DT)+\frac{\partial}{a\cos^2\theta\partial\theta}(n\phi|D|DS\cos^2\theta)\right\}$$

$$F_\theta=2(k_0 a\Delta\theta)^2\left\{\frac{\partial}{a\cos\theta\partial\lambda}(n\phi|D|DS)-\frac{\partial}{a\cos^2\theta\partial\theta}(n\phi|D|DT\cos^2\theta)\right\} \quad (4.15)$$

where k_0 is a constant having a value between 0.1 and 1.0. In the formulation of (4.15), the wave number of the largest unresolvable eddy is assumed to be $\{(2a\cos\theta\Delta\lambda)^{-2}+(2a\Delta\theta)^{-2}\}^{1/2}/k_0=(\sqrt{2}ak_0\Delta\theta\cdot\sqrt{n})^{-1}$ where $n=2/\{1+(\Delta\theta/\cos\theta\,\Delta\lambda)^2\}$. DT and DS are tension and shearing rates of strain, respectively, i.e.,

$$DT=\frac{\partial u}{a\cos\theta\partial\lambda}-\frac{\cos\theta}{a}\frac{\partial}{\partial\theta}\left(\frac{v}{\cos\theta}\right)$$

$$DS=\frac{\partial v}{a\cos\theta\partial\lambda}+\frac{\cos\theta}{a}\frac{\partial}{\partial\theta}\left(\frac{u}{\cos\theta}\right)$$

and $|D|=\{(DS)^2+(DT)^2\}^{1/2}$ is pure deformation. We can compute DT, DS, and D in System 3 from u and v in Systems 1 and 2. For instance, referring to figure 3, we obtain

$$DT_K=\alpha_1\frac{\cos\theta_j}{\cos\theta_{j-1/2}}\left\{\frac{u_A+u_Y}{2}-\frac{u_B+u_Z}{2}\right\}-\alpha_3\cos\theta_{j-1/2}\left\{\frac{v_Y+v_Z}{2\cos\theta_{j-1}}-\frac{v_A+v_B}{2\cos\theta_j}\right\}$$

$$DS_K=\alpha_1\frac{\cos\theta_j}{\cos\theta_{j-1/2}}\left\{\frac{v_A+v_Y}{2}-\frac{v_B+v_Z}{2}\right\}+\alpha_3\cos\theta_{j-1/2}\left\{\frac{u_Y+u_Z}{2\cos\theta_{j-1}}-\frac{u_A+u_B}{2\cos\theta_j}\right\}$$

$$|D|_K=\{(DT_K)^2+(DS_K)^2\}^{1/2}$$

where α_1 and α_3 are the same as those defined in (4.12). Then, F_λ and F_θ are given by

$$(F_\lambda)_{i,j}\approx 2(k_0 a\Delta\theta)^2\left[\alpha_1 n_j(\phi_E|D|_E DT_E-\phi_W|D|_W DT_W)+\alpha_2\frac{1}{\cos\theta_j}\{(\phi|D|DS)_N n_{j-1/2}\cos^2\theta_{j-1/2}-(\phi|D|DS)_S n_{j+1/2}\cos^2\theta_{j+1/2}\}\right] \quad (4.16)$$

$$(F_\theta)_{i,j}\approx 2(k_0 a\Delta\theta)^2\left[\alpha_1 n_j(\phi_E|D|_E DS_E-\phi_W|D|_W DS_W)-\alpha_2\frac{1}{\cos\theta_j}\{(\phi|D|DT)_N n_{j-1/2}\cos^2\theta_{j-1/2}-(\phi|D|DT)_S n_{j+1/2}\cos^2\theta_{j+1/2}\}\right] \quad (4.17)$$

where α_2 is defined in (4.12). In (4.16) and (4.17), n_j is a factor related to an area element centered at the point A in figure 4, $n_{j-1/2}$ and $n_{j+1/2}$ are related to the corresponding areas centered at the points K and P in figure 3, respectively; these are written

$$n_j=2/\{1+(\Delta\theta/\cos\theta_j\Delta\lambda_j)^2\}$$

$$n_{j-1/2}=2/\{1+(\Delta\theta/\cos\theta_{j-1/2}\Delta\lambda_j)^2\}$$

$$n_{j+1/2}=2/\{1+(\Delta\theta/\cos\theta_{j+1/2}\Delta\lambda_{j+1})^2\}$$

We also made test runs with linear viscosity. In this case, F_λ and F_θ are estimated by (4.18)

$$F_\lambda=A\left\{\frac{\partial}{a\cos\theta\partial\lambda}\left(\phi\frac{\partial u}{a\cos\theta\partial\lambda}\right)+\frac{\partial}{a\cos^2\theta\partial\theta}\left(\phi\cos^2\theta\frac{\partial u}{a\partial\theta}\right)\right\}$$

$$F_\theta=A\left\{\frac{\partial}{a\cos\theta\partial\lambda}\left(\phi\frac{\partial v}{a\cos\theta\partial\lambda}\right)+\frac{\partial}{a\cos\theta\partial\theta}\left(\phi\cos\theta\frac{\partial v}{a\partial\theta}\right)\right\} \quad (4.18)$$

where A is the kinematic eddy-viscosity coefficient. F_λ is derived by dividing the eddy diffusion of relative angular momentum by $a\cos\theta$. F_θ represents the diffusion of v-momentum. The finite difference forms of (4.18) are given by

$$(F_\lambda)_{i,j}\approx A\left[\alpha_1\left\{\phi_E\left(\frac{\partial u}{a\cos\theta\partial\lambda}\right)_E-\phi_W\left(\frac{\partial u}{a\cos\theta\partial\lambda}\right)_W\right\}+\frac{\alpha_2}{\cos\theta_j}\left\{\left(\phi\frac{\partial u}{a\partial\theta}\right)_N\cos^2\theta_{j-1/2}-\left(\phi\frac{\partial u}{a\partial\theta}\right)_S\cos^2\theta_{j+1/2}\right\}\right] \tag{4.19}$$

$$(F_\theta)_{i,j}\approx A\left[\alpha_1\left\{\phi_E\left(\frac{\partial v}{a\cos\theta\partial\lambda}\right)_E-\phi_W\left(\frac{\partial v}{a\cos\theta\partial\lambda}\right)_W\right\}+\alpha_2\left\{\left(\phi\frac{\partial v}{a\partial\theta}\right)_N\cos\theta_{j-1/2}-\left(\phi\frac{\partial v}{a\partial\theta}\right)_S\cos\theta_{j+1/2}\right\}\right] \tag{4.20}$$

Here, $(\partial u/a\cos\theta\,\partial\lambda)_E$, $(\phi\partial u/a\partial\theta)_N$, etc., are obtained from ϕ and the values of $(\partial u/a\cos\theta\,\partial\lambda)$, $(\partial u/a\partial\theta)$, etc., in System 3. The latter quantities are estimated by the following schemes. (Refer to fig. 3.)

$$\left(\frac{\partial u}{a\cos\theta\partial\lambda}\right)_K\approx\alpha_1\frac{\cos\theta_j}{\cos\theta_{j-1/2}}\left\{\frac{u_A+u_Y}{2}-\frac{u_B+u_Z}{2}\right\}$$

$$\left(\frac{\partial u}{a\partial\theta}\right)_K\approx\alpha_3\left\{\frac{u_Y+u_Z}{2}-\frac{u_A+u_B}{2}\right\}$$

As we mentioned before, the initial data used in our test are the same as given by Phillips [7]. Namely, the initial field of wind velocity is obtained from the stream function of a Haurwitz-type wave with wave number 4, i.e., equation (36) with $R=4$ in Phillips' paper. The initial field of geopotential is given by equation (38) in his paper. The fields of geopotential and stream function satisfy the so-called balance condition. In the case of the initial fields that we used, the predictions in one quarter of the Northern Hemisphere repeat in the other three quarters and those in the Southern Hemisphere are symmetrical to the Northern Hemisphere. The computations were made only for a quarter of the Northern Hemisphere by assuming a cyclic field in the longitudinal direction, a symmetric field with respect to the equator, and a calm condition at the north pole.

The equations were integrated by three schemes. Hereafter, u^τ, v^τ, ϕ^τ, $U^\tau(=u^\tau\phi^\tau)$, $V^\tau(=v^\tau\phi^\tau)$ represent the values at the time level τ, and G_λ^τ, G_θ^τ, F_λ^τ, F_θ^τ, and H^τ are the values of G_λ, etc., estimated from u^τ, v^τ and ϕ^τ. u^*, G_λ^*, F_λ^*, etc., are used with a similar meaning to denote the values at the first step iteration. Double asterisks indicate the second step iteration. Then, the integration schemes of U and ϕ are written as follows. (A scheme for V is omitted as it is similar to that for U.)

Scheme A (leapfrog method):

$$\begin{cases}U^{\tau+1}=U^{\tau-1}+2\Delta t(G_\lambda^\tau+F_\lambda^{\tau-1})\\ \phi^{\tau+1}=\phi^{\tau-1}+2\Delta tH^\tau\end{cases}$$

Scheme B (modified Euler-backward iteration):

$$\left.\begin{cases}U^*=U^\tau+\frac{\Delta t}{2}G_\lambda^\tau\\ \phi^*=\phi^\tau+\frac{\Delta t}{2}H^\tau\end{cases}\right\}\quad\text{(modified Euler method)}$$

$$\begin{cases}U^{**}=U^\tau+\Delta tG_\lambda^*\\ \phi^{**}=\phi^\tau+\Delta tH^*\end{cases}$$

$$\begin{cases}U^{\tau+1}=U^\tau+\Delta t(G_\lambda^{**}+F_\lambda^\tau)\\ \phi^{\tau+1}=\phi^\tau+\Delta tH^{**}\end{cases}\quad\text{(backward correction)}$$

Scheme C (leapfrog-trapezoidal iteration):

$$\begin{cases}U^*=U^{\tau-1}+2\Delta tG_\lambda^\tau\\ \phi^*=\phi^{\tau-1}+2\Delta tH^\tau\end{cases}\quad\text{(leapfrog method)}$$

$$\begin{cases}U^{\tau+1}=U^\tau+\frac{\Delta t}{2}(G_\lambda^\tau+G_\lambda^*)+\Delta tF_\lambda^\tau\\ \phi^{\tau+1}=\phi^\tau+\frac{\Delta t}{2}(H^\tau+H^*)\end{cases}\quad\text{(trapezoidal correction)}$$

We used a time step $\Delta t=10$ min. here. The Courant-Friedlich-Levy condition is satisfied with this value and the specified resolution $N=20$, the meridional increment for which is 500 km. The characteristics of the above schemes have been discussed by the author [4]. Scheme B is free from a computational mode. A selective damping of gravitational waves is a feature of scheme B. A computational mode is suppressed to a high degree by Scheme C. In order to apply Scheme A or C to obtain the values at $t=\Delta t$, we need a special process. In test runs, we used forward time differences to get the values at $t=\Delta t/2$ first. Then Scheme A or C was used with the time step replaced by $\Delta t/2$.

5. RESULTS AND ANALYSES OF THE TEST RUNS

Table 3 is a list of the test runs we made. Run 1 has no prevention against a computational mode, gravitational waves, and destructive short waves. The other runs were attempted to suppress, more or less, the trouble

TABLE 3.—*A list of the test runs. All runs were made with* N=*20 and* Δt=*10 min. Time integration schemes are explained near the end of section 4.* k₀ *is a constant in the non-linear viscosity term (4.15).* A *is a kinematic eddy viscosity coefficient in the linear viscosity term (4.18)*

Run	Integration scheme	k_0 or A	Computation time (min.)
1	Scheme A	no viscosity term	36
2	Scheme B	no viscosity term	81
3	Scheme C was used for 3 steps every 12 hr. Scheme A was used for the other steps.	no viscosity term	37
11	Scheme A	$k_0=0.1$	52
12	Scheme A	$k_0=0.2$	52
13	Scheme A	$k_0=0.3$	52
14	Scheme A	$k_0=0.5$	52
21	Scheme A	$A=10^5$ m.² sec.⁻¹	43
22	Scheme A	$A=5\times10^5$	43
23	Scheme A	$A=10^6$	43

resulting from the above factors. In the last column, the total computation time for a 16-day prediction on the IBM 7030 (STRETCH) is shown for each run. As the prediction and the analysis were made in a single program, the time used for analysis was also included in this figure.

As discussed by Phillips [7], gravitational oscillations are caused from the beginning of the integration not by the numerical technique but by our choice of initial fields. But the behavior of the flow pattern for a few days will resemble the barotropic non-divergent forecast starting with the same field of stream function as we chose. In the latter case, the pattern moves to the east while preserving the initial shape. In all test runs, the average speed of eastward movement of the pattern for four days was about 11° of longitude per day. This is a little slower than the speed for the non-divergent case. We could see no sign of distortion or tearing of the flow pattern, which has been a deficiency of spherical grid methods used by Kuo and Nordö [3] and by Gates and Riegel [1, 2]. As the latitudinal change of zonal increment in the newly designed grid system is gradual, there is not a latitudinal jump in the retardation of waves resulting from the space truncation error. At about the fifth day, a small-scale wave appeared in Runs 1, 3, 11, and 21, and it continued to grow with time. In these runs the fields in time became less smooth as the number of marching steps increased. It was, however, easy in every run to trace the movement of the major trough in the flow pattern until the end of the integration period. The integration was terminated at the end of the 16th day, i.e., at 2304 steps, even in the run in which there was no numerical difficulty to prevent extending the integration.

We have, from (3.3), (4.13), and (4.14),

$$\sum_j \sum_i \frac{\rho}{g} H_{i,j} \Delta S_j = 0 \qquad (5.1)$$

where the summation is taken for the entire grid, and ρ is the density of the air. Equation (5.1) means that the total mass of the air is conserved. In a similar way, from (3.3), (4.10), (4.13), and (4.16) (or (4.19)), we have

$$\sum_j \sum_i \frac{\rho}{g} \left\{ \frac{\cos\theta_{j-1/2} + \cos\theta_{j+1/2}}{2} a(G_\lambda + F_\lambda)_{i,j} + \frac{\cos^2\theta_{j-1/2} + \cos^2\theta_{j+1/2}}{2} a^2 \Omega H_{i,j} \right\} \Delta S_j = \epsilon \qquad (5.2)$$

Here, ϵ represents a leak of relative angular momentum at the northern boundary of the zonal ring of $j=2$ to or from the small polar cap ($j=1$). This ϵ has no counterpart, as we assumed $u=0$ at $j=1$. Equation (5.2) shows that, if we define the total absolute angular momentum by

$$\sum_j \sum_i \frac{\rho}{g} \left\{ \frac{\cos\theta_{j-1/2} + \cos\theta_{j+1/2}}{2} a u_{i,j} + \frac{\cos^2\theta_{j-1/2} + \cos^2\theta_{j+1/2}}{2} a^2 \Omega \right\} \phi_{i,j} \Delta S_j \qquad (5.3)$$

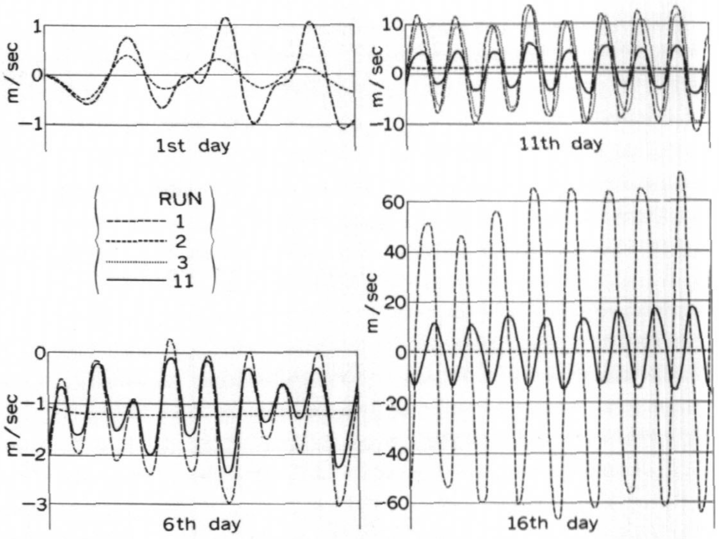

FIGURE 6.—The variation of meridional component of wind with time at Point (2,3). The plot is made for the 1st, the 6th, the 11th, and the 16th days.

it will be almost conserved. In the test computations, the magnitude of the fluctuation of absolute angular momentum as defined by (5.3) was indeed very small. Namely, it was within 10^{-3} percent of the initial value of the total absolute angular momentum in Runs 21, 22, and 23, and within 10^{-4} percent in the other runs.

We made an analysis of the high-frequency oscillation, computational mode, and short waves by comparisons of the results of Runs 1, 2, 3, and 11. As described before, Run 1 was affected by all of these three undesirable elements. In some cases, high-frequency oscillation in the solution of primitive equations is a numerically caused noise. It may be necessary to control it when it is excited. In Run 2, we intended to suppress it through the use of the iterative time integration scheme which could cause a highly selective damping of it. We tried to eliminate only the computational mode in Run 3. Run 11 was supposed to cause a weak damping of short waves. Let us examine, first, a variation of a quantity with time at specified grid points. Figure 6 is a plot of the meridional component of wind for the 1st, 6th, 11th, and 16th day at Point (2, 3), which is very near the pole. A plot for Run 3 is made only for the 11th day and that for Run 11 for the 1st day is omitted. In Run 2, the prediction of v at this point was very stable and the amplitude of its variation was small. Even on the 16th day, it only varied between 23 cm. sec.$^{-1}$ and −57 cm. sec.$^{-1}$ But in Run 1, a high-frequency oscillation with a period of about 3 hr. developed with time. Its amplitude on the 6th, the 11th, and the 16th day was 1 m. sec.$^{-1}$, 10 m. sec.$^{-1}$, and 50 m. sec.$^{-1}$, respectively. The amplitude for Run 3 on the 11th day was about 90 percent of that for Run 1. We made comparisons between the results of these two runs from many aspects. We can conclude that, so far as the test computation was concerned, the

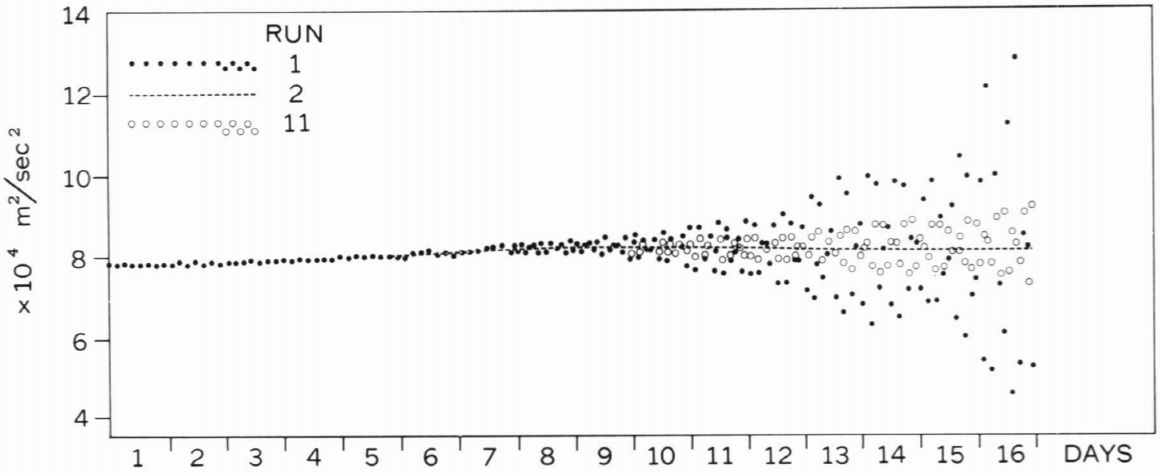

FIGURE 7.—The variation of geopotential at the pole with time. Plot is made for every 10 steps for Run 1 (the whole period) and for Run 11 (after the 1300th step). Curve for Run 2 is drawn after the 700th step.

amplitude of the computational mode was very small. The plot for Run 11 in figure 6 suggests that the high-frequency oscillation could be controlled to some degree by suppressing short waves. This will be reaffirmed later.

The variation of geopotential at the pole, i.e., at a singular point, is shown in figure 7. The geopotential at the pole did not oscillate in Run 2. But in Run 1, an oscillation became noticeable at about the 1000th step and its amplitude increased with time. These features coincide quite well with the above-mentioned analyses of the v-field near the pole.

In order to show how a high-frequency oscillation appears in the middle latitudes and on the equator, figures 8 and 9 are presented. In figure 8, a plot of geopotential at Point (6, 11) is made. The location of this point is almost the same as that of Point II in Phillips' [7] analysis. Figure 9 illustrates the variation of geopotential at Point (11, 21), i.e., on the equator. We again observe a damping of the gravitational wave in Run 2, its growth in Run 1, and a relatively small oscillation in Run 11. As seen in figure 8, the gravitational wave was almost completely suppressed within the first day. Comparing figures 6 through 9, we can say that in Run 1 a high-frequency oscillation is superposed on the curve corresponding to Run 2. This means that (1) the gravitational wave could be eliminated by the time integration scheme used in Run 2 with little effect on the prediction of the trend of the meteorological wave, and (2) the interaction between the gravitational wave and the meteorological wave was small in the test computation.

The growth of short waves can be revealed by a spectrum analysis. Table 4 shows amplitudes of the Fourier series of geopotential along the 13th latitude circle (36° lat.) for various runs. The average spectra for the 6th and the 16th day are listed. It is seen that the growth of the tail end of the spectrum in Run 11 was smaller than in Run 1 and Run 2. This is probably the effect of viscosity, although it seems too weak to suppress the growth of short

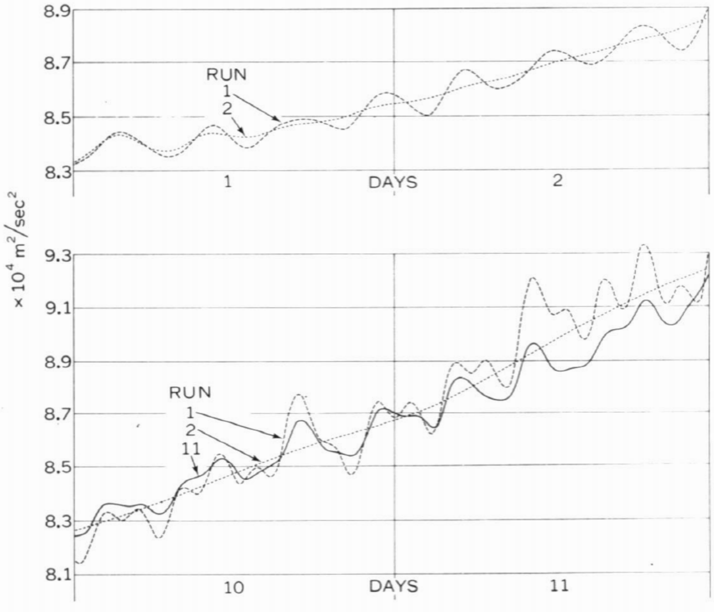

FIGURE 8.—The variation of geopotential at Point (6,11) with time.

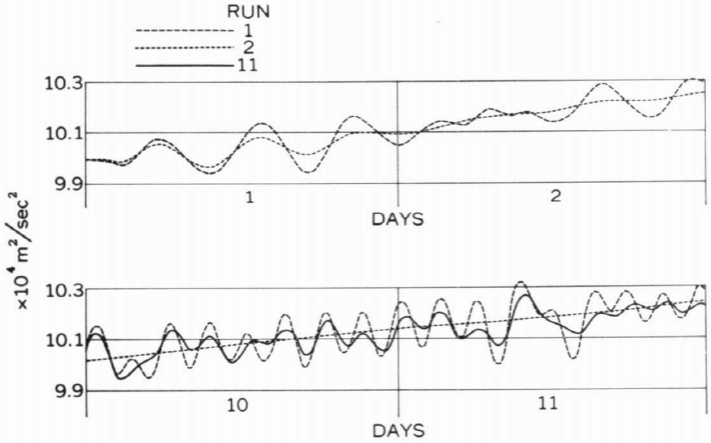

FIGURE 9.—The variation of geopotential at Point (11,21) with time.

TABLE 4.—*Amplitudes of the Fourier series of the geopotential along the 13th latitude (36° lat.). Fourier analysis was made for a range of 90° long. The average spectra for the 6th and the 16th day are shown (in 10^3 m.²/sec.²)*

Period	6th day						16th day					
Wave number..	1	2	3	4	5	6	1	2	3	4	5	6
Run 1	6.91	0.14	0.12	0.29	0.75	0.49	5.16	1.84	1.71	2.16	6.32	3.49
2	6.89	0.06	0.13	0.32	0.59	0.49	5.72	1.81	1.40	1.47	3.09	2.12
11	6.53	0.12	0.10	0.20	0.48	0.45	5.85	0.92	0.71	1.13	2.95	1.70
14	2.57	0.03	0.07	0.07	0.10	0.06	1.51	0.08	0.07	0.04	0.16	0.06

waves completely. It should be noted that short waves, which had nothing to do with high-frequency oscillations, developed in Run 2.

As shown above, there are two kinds of short waves. We denote these by HS (high frequency short waves) and LS (low frequency short waves). For the long waves, too, we have HL (high frequency long waves) and LL (low frequency long waves). The LL wave is the so-called meteorological wave. We assume that a geopotential field at any instant consists of the above four components. Then, the contribution of each component to the tendency of geopotential at one point is proportional to the amplitude of this component multiplied by its phase velocity times the inverse of its wavelength. Accordingly, an HS wave, if there is one, has a large weight in the tendency of geopotential.

As a measure of the magnitude of the tendency, we computed a global average of $|\phi^{\tau+1}-\phi^{\tau}|$. Figure 10 is a plot of this quantity for Runs 1 and 2. Since the geopotential field was smooth initially, we may say that the HS and LS waves were negligible in the beginning. As we mentioned before, the HL wave was caused from the beginning in our case. Hence, the level B in figure 10 shows the sum of the contributions of the HL and the LL waves. Since the HL wave was damped early in Run 2, the level A in figure 10 shows the contribution of the LL wave. The difference of the levels A and B can be attributed to the HL wave. We further assume that the contributions from the LL and the HL waves did not change throughout the whole period. Then, the difference between the plot for Run 2 and the level A was caused by the LS wave. The difference between the plots for Runs 1 and 2 shows the sum of the effects of the HL and the HS waves. We can, therefore, estimate the contributions from the LL, HL, LS, and HS waves in Run 1. In the units m.² sec.$^{-2}$ (10 min.)$^{-1}$, they are 14:28:0:0 in the beginning, 14:28:5:180 for the 11th day, and 14:28:17:820 for the 16th day, respectively. The troublesome behavior of the HS wave is clearly shown.

Although the integration Scheme B, which we used in Run 2, could eliminate the HS wave very well, it was not effective for suppressing the LS wave. The growth of the LS wave may be a source of trouble in a long run, e.g., a cause of aliasing. We attempted to control this wave by viscosity, which might cause the dissipation of the HS wave too. Furthermore, an introduction of viscosity will result in more or less a damping of long waves, and, hence, a weakening of the production of short waves through non-linear interactions. We performed three more integrations (Runs 12, 13, and 14) using the same computation schemes both in space and time as in Run 11, but changing the constant in the viscosity terms (4.15). Use of a large constant was indeed effective for suppressing both the HS and the LS waves. For example, table 4

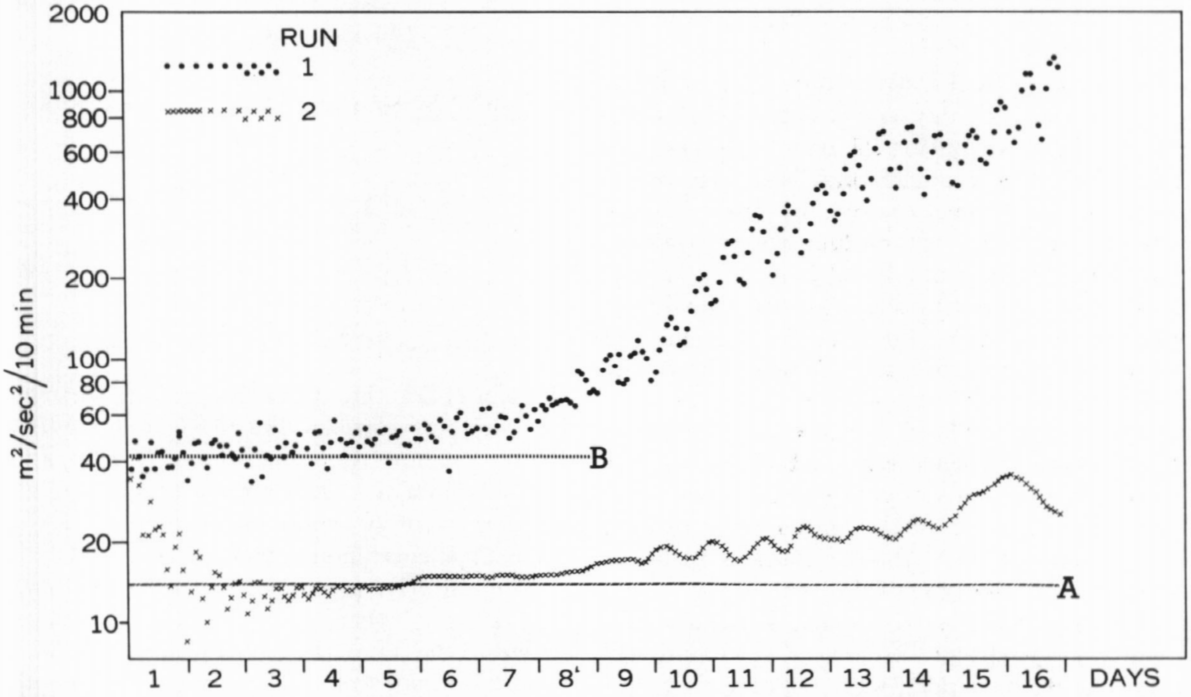

FIGURE 10.—The variation of a global average of $|\phi^{\tau+1}-\phi^{\tau}|$ with time. Plot is made for every 10 steps. The level A shows the contribution of the LL wave to the tendency. The level B represents the sum of the contributions from the LL wave and the HL wave.

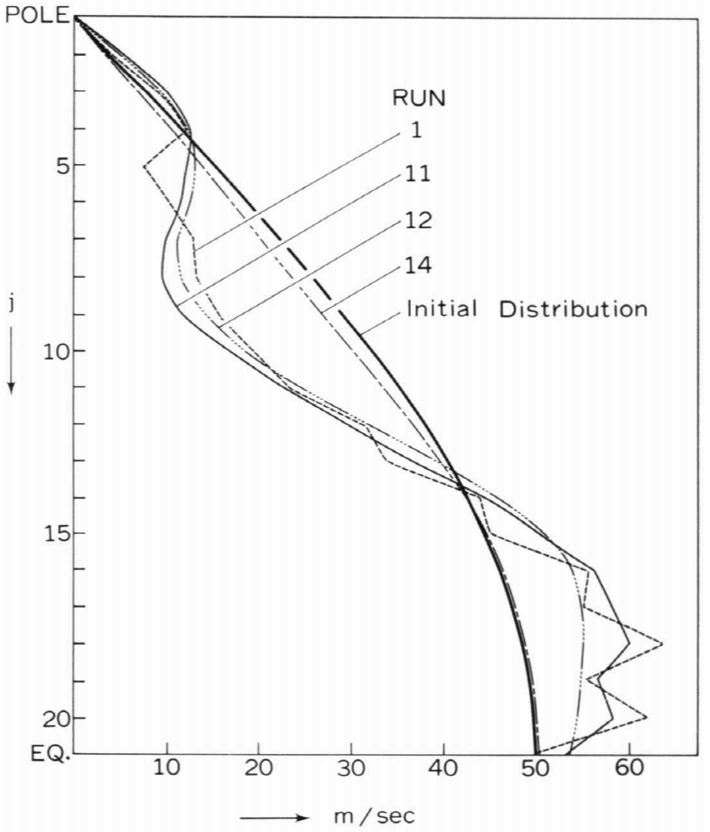

FIGURE 11.—The latitudinal distributions of zonal mean of u at the end of the 10th day. Those for Runs 1, 11, 12, and 14 are shown. The initial distribution is also shown.

shows that the tail end of the spectrum of geopotential did not grow in Run 14. But, in this run, a strong diffusion of momentum made the flow pattern different from the case of weak viscosity.

In figure 11, the latitudinal distributions of zonal mean of u at the end of the 10th day are illustrated for Runs 1, 11, 12, and 14. The distribution for Run 14 differs from the others. It is hard to say which run is best. However, if we intend to eliminate short waves by the viscosity which has the smallest effect on the long waves, the viscosity used in Run 14 may not be appropriate for this purpose. If viscosity works in the way we intend, the LL and the HL waves in Run 1 remain almost unchanged while the short waves are filtered. Consequently, the value $|\phi^{\tau+1}-\phi^{\tau}|$ will maintain the level B of figure 10.

To reduce this level to the level A in the same figure we must adopt the integration scheme B. At that time, the HL wave is damped out and we have the LL wave only. Figure 12 shows the variation of the above measure with time for Runs 11 through 14. About 0.2 seems to be an optimum value of k_0 for the type of flow pattern we used. In the case of a more complicated model, especially in a baroclinic model, the shape of the energy spectrum will differ from the one we have dealt with. There may be a supply of energy to the waves of specific scale. Accordingly, the optimum value of k_0 may be different.

Here, we mention briefly an analysis of the energy budget. From (4.7), (4.8), and (4.9) with the viscosity terms added, we have

$$\frac{\partial K}{\partial t}=C+E$$

$$\frac{\partial P}{\partial t}=-C \qquad (5.4)$$

where $K=\rho/g\int\int\frac{1}{2}(u^2+v^2)\phi dS$ is total kinetic energy, $P=\rho/g\int\int\frac{1}{2}\phi^2 dS$ is total potential energy. Here, C and E are the conversion of potential to kinetic energy and the dissipation of kinetic energy respectively,

$$C=-\rho/g\iint\phi\mathbf{V}\cdot\nabla\phi\, dS$$

$$E=\rho/g\iint(uF_\lambda+vF_\theta)dS$$

If we define as follows

$$u_*=\frac{u_N+u_S}{2}$$

$$\phi_*=\frac{\phi_N+\phi_S}{2}$$

$$v_*\phi_*=\frac{(v\phi)_N\cos\theta_{j-½}+(v\phi)_S\cos\theta_{j+½}}{\cos\theta_{j-½}+\cos\theta_{j+½}}$$

$(4.10)\times u_*+(4.11)\times v_*$ leads to a vanishing of the work due to the Coriolis force. Using u_*, v_*, and ϕ_*, we evaluated K, P, C, and E by the following numerical integration,

$$K\approx\rho/g\sum_j\sum_i\frac{1}{2}\{u_*^2+v_*^2\}\phi_*\Delta S_j$$

$$P\approx\rho/g\sum_j\sum_i\frac{1}{2}\phi_*^2\Delta S_j$$

$$C\approx-\rho/g\sum_j\sum_i\left\{u_*\alpha_1\frac{\phi_E+\phi_W}{2}(\phi_E-\phi_W)+v_*\alpha_3\frac{\phi_E+\phi_W}{2}(\phi_N-\phi_S)\right\}\Delta S_j$$

$$E\approx\rho/g\sum_j\sum_i\{u_*(F_\lambda)_{i,j}+v_*(F_\theta)_{i,j}\}\Delta S_j$$

We can check the above integration schemes by examining whether relations like (5.4) hold numerically or not. Figure 13 shows time histories of K, P, C, and $|E|$ for Run 12 for two days. (E is always negative.) It is seen that an increase of K occurs only when $C>|E|$, and the variation of P corresponds well to that of C. These are in good qualitative agreement with (5.4). It was also found that, although there was a slight quantitative discrepancy between the numerical estimations of the left- and the right-hand sides of (5.4), it could be smoothed out in a budget analysis for a long period. The time integration Schemes B and C have damping characteristics by themselves. But the rate of damping was not large in the test runs. The initial values of K and P for the Northern Hemisphere were 3.6×10^{21}, 1.2×10^{23} (in m.-kg.-sec. units), respectively. Table 5 shows the ratio of $(K+P)$ at the end of the 16th day to its initial value, the final level of K, the initial and the final levels of $|E|$, and the dissipation rate of kinetic energy near the end of the integration period. In Runs 12 through 14, the decrease of the level of K is seen. The dissipation of kinetic energy by the non-linear viscosity for a given grid size is proportional to k_0^2 times the cube of the magnitude of pure deformation. Therefore, at the beginning of integration, the dissipation was very large in runs with large k_0. Later, it became small compared with the case of small k_0, because of a considerable decrease in deformation. Column (5) of table 5 shows that the rate of dissipation of kinetic energy at the 16th day was about 1 percent per day in Runs 11 through 14. This, however, does not mean the dissipation rate approaches a small value in the integration for an atmospheric model in general. In the case of a baroclinic model, the development of unstable waves may offset the decrease of the deformation field by viscosity. Consequently, the dissipation rate of kinetic energy will be maintained at a much higher level than the present estimation.

We made other test computations, Runs 21, 22, and 23. In these runs, the linear viscosity term (4.18) was applied instead of (4.15). Other computation schemes are the same as we used in the runs with non-linear viscosity. The average space increment for the resolution $N=20$ is about 600 km. Introducing $l=6\times10^7$ cm. into Richardson's empirical law $A=0.2l^{4/3}$, we have $A=5\times10^5$ m.^{2} sec.$^{-1}$. This value was adopted as the kinematic eddy-viscosity coefficient in Run 22. The smaller value, i.e., $A=10^5$ m.^{2} sec.$^{-1}$, was used in Run 21, and the larger value, $A=10^6$ m.^{2} sec.$^{-1}$ was applied to Run 23.

TABLE 5.—*Column (1): the ratio* (K+P) *at the end of the 16th day to its initial value (in percent). Column (2): the final level of* K *(in 10^{21} m.-kg.-sec. units). Column (3): the initial level of* |E| *(in 10^{17} m.-kg.-sec. units per 10 min.). Column (4): the final level of* |E| *(in 10^{17} m.-kg.-sec. units per 10 min.). Column (5): dissipation rate of kinetic energy near the end of 16th day (in percent per day)*

	(1) $\frac{(K+P)\ \text{16th}}{(K+P)\ \text{1st}}$	(2) K 16th day	(3) $\|E\|$ 1st day	(4) $\|E\|$ 16th day	(5) $\frac{\|E\|\ \text{16th}}{K\ \text{16th}}$
Run 1	101.3	4.6			
2	100.4	4.2			
11	99.8	3.7	2.5	3.0	1.2
12	99.2	2.9	10	2.0	1.0
13	99.0	2.5	22	1.3	0.8
14	98.8	2.2	62	0.4	0.3
21	99.9	3.6	1.3	2.0	0.8
22	99.3	3.0	6.4	2.5	1.2
23	99.0	2.5	13	2.1	1.2

As we have mentioned before, the variation of the magnitude of the tendency of geopotential with time is a good measure to show how the short waves developed or were suppressed. We made a plot for each run in the same way as we did in figures 10 and 12. The trend of the plot for Run 21 was between those for Runs 1 and 11. Namely, the growth of the short waves could not be suppressed in Run 21. In the case of Run 22, the plot before the 10th day was seen around the line corresponding to level B in figure 12. The plot after the 11th day was

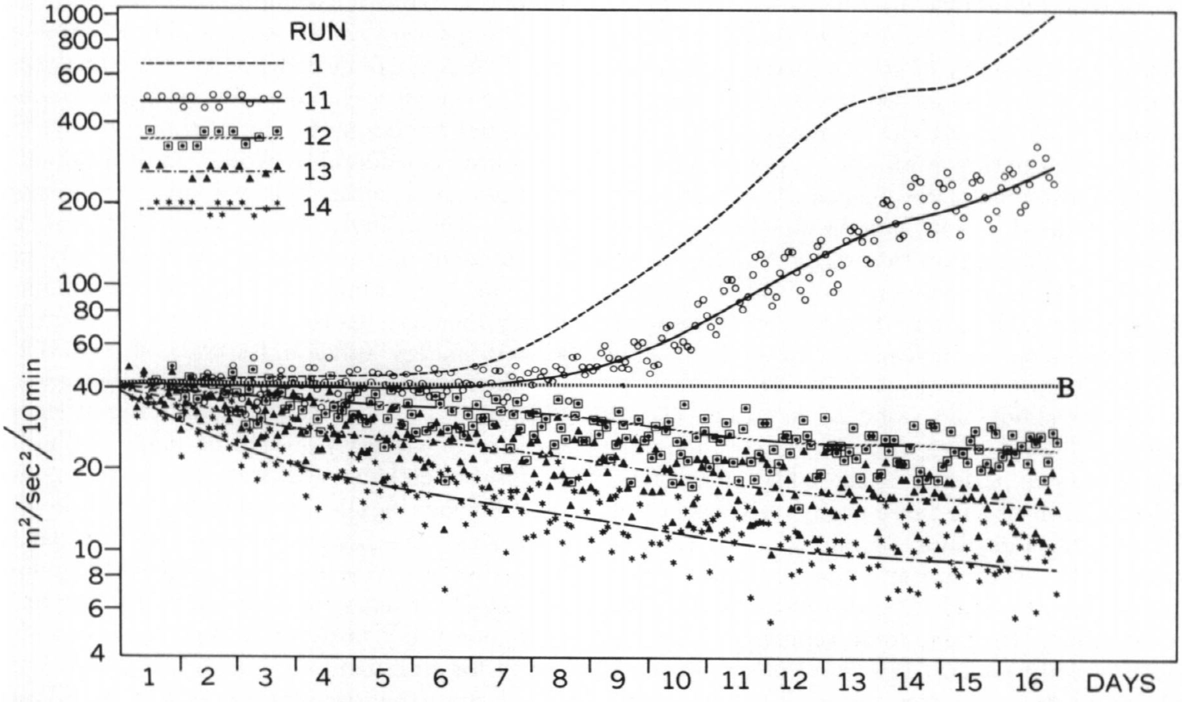

FIGURE 12.—The variation of a global average of $|\phi^{\tau+1}-\phi^{\tau}|$ with time. Plot is made for every 10 steps. The level B is the same as in figure 10.

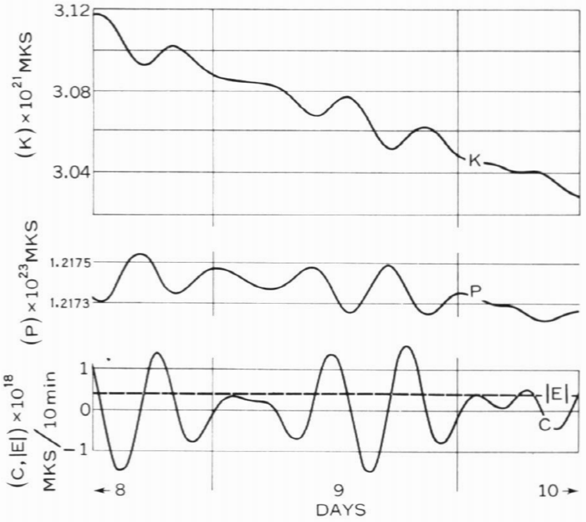

FIGURE 13.—Time histories of K (total kinetic energy), P (total potential energy), C (conversion of potential energy to kinetic energy), and $|E|$ (dissipation of kinetic energy). The variation in Run 12 is shown for a 48-hr. period.

slightly above the level B. The plot for Run 23 showed a trend corresponding to Run 13. Consequently, it was shown that the use of the linear viscosity also could suppress the growth of the short waves. The optimum value of the eddy-viscosity coefficient for numerically stabilizing this test computation is a little larger than 5×10^5 m.^{2} sec.$^{-1}$.

Finally, we consider the effects of viscosities of different types and different amounts.

The first problem is the comparison between the test runs with non-linear viscosity and those with linear viscosity. We have stated above that Runs 21, 22, and 23 showed a trend similar to Runs 11, 12, and 13, respectively, in the analysis of the tendency of geopotential. The same correspondences are also seen in the energy analysis which is shown in table 5. At the beginning of the integration period, the dissipation of kinetic energy in Runs 21, 22, and 23 is proportional to the magnitude of the eddy-viscosity coefficient used. But, as a result of the change of the wind field, the dissipation rate of the kinetic energy at the end of the 16th day (column (5)) in all three runs is almost the same, i.e., it is about one percent per day. This situation is the same as in Runs 11, 12, and 13. The final level of the kientic energy in Runs 21, 22, and 23 (column(2)) is also about the same as in Runs 11, 12, and 13, respectively.

TABLE 6.—*Differences between the maximum and the minimum values of* u, v *and* ϕ *on the specified latitudes at the end of the 10th day*

Group	Run	u (m. sec.$^{-1}$)			v (m. sec.$^{-1}$)			ϕ (10^3 m.^{2} sec.$^{-2}$)		
		$j=4$	12	21	$j=4$	12	20	$j=4$	12	21
A	Run 11	15.2	54.4	61.6	11.2	100.8	18.7	0.4	13.6	2.1
	Run 21	15.9	59.1	67.4	12.2	104.3	19.6	1.0	14.1	2.4
B	Run 12	9.4	33.8	45.8	7.1	81.3	15.3	0.6	10.5	1.3
	Run 22	9.9	39.0	46.3	7.5	84.1	15.8	0.6	11.0	1.4
C	Run 13	5.3	22.1	38.0	4.7	59.3	12.3	0.2	6.9	1.1
	Run 23	6.2	25.3	36.7	4.9	65.2	12.5	0.2	8.1	0.9
D	Run 14	2.6	12.5	23.1	1.8	29.8	7.2	1.6	3.5	1.1

We further made comparisons of the eddy parts of the field quantities in each of the three groups: Runs 11 and 21, Runs 12 and 22, and Runs 13 and 23. In table 6, the differences of the maximum and the minimum values of u, v and ϕ on the specified latitudes at the end of the 10th day are shown. Roughly, these represent twice the amplitudes of the eddy parts. We again observe a good agreement between the two runs in each group. This means that the level of the eddy kinetic energy is almost the same in the two runs. As for the zonal mean quantity, we compared the latitudinal distribution of the zonal mean of u at the end of the 10th day in Runs 21, 22, and 23 with figure 11. The distributions were seen near the lines for Runs 11 or 12 in figure 11, except for a portion of $j=2$ and 3. At the very high latitudes, the zonal mean of u in the runs with linear viscosity was about twice that in the runs with non-linear viscosity. This is perhaps due to the different effects of viscosities of different types. We have already mentioned that the fluctuation of the total absolute angular momentum defined by (5.3) is caused by the leak of the momentum to or from the small polar cap and it is relatively large in Runs 21–23 compared with Runs 11–14, though it is still negligible. On the whole, so far as our test computations are concerned, the behavior of the runs with non-linear viscosity with the coefficient $k_0=0.1$, 0.2, and 0.3 resembles quite well that of the runs with linear viscosity with $A=10^5$, 5×10^5, and 10^6 m.^{2} sec.$^{-1}$, respectively.

The next problem is the comparison among the runs with different amounts of viscosity. Based on the discussions above, we classified the test runs into four groups as shown in table 6 according to the behavior of the integration. We can assume that the different results among the groups were caused by the different amounts of viscosity. Then, it can be deduced from the analyses made so far, that as the viscosity increases from the amount for Group A to that for Group C, the level of the eddy kinetic energy decreases considerably while the latitudinal distribution of the zonal mean relative angular momentum varies little. Accordingly, the amount of the viscosity has much effect on the ratio between the eddy kinetic energy and the zonal kinetic energy. If the amount of the viscosity increases to that for Group D (Run 14), the eddy kinetic energy takes a lower level and the distribution of the zonal mean relative angular momentum also changes. It seems that the determination of the proper amount of viscosity should be made in the future on the basis of the theoretical and observational understanding of diffusion in the atmosphere, and the results of the numerical integration should be compared with the evolution of a wave and the budgets of angular momentum and kinetic energy in the actual atmosphere.

In our test computation, the optimum amount of viscosity for stabilizing the numerical integration was a little larger than the viscosity for Group A. All the test runs with viscosity were integrated with the leapfrog method. If we use an iterative integration method, the optimum value of viscosity may be different, as the high-frequency part of the short wave is damped through the integration. At any rate, it is to be noted that the optimum amount of viscosity must not be larger than the proper amount which represents the actual diffusion process in the atmosphere. If this condition is satisfied, we will be justified in utilizing the viscosity term in the equations for suppressing growth of the short waves. If it is not satisfied, we should use another method to control the short waves, e.g., a filtering of the components of high wave number in the data at times during the integration, or we should consider other computation procedures since the behavior of short waves greatly depends on the finite difference schemes.

We have attempted to investigate the effects of viscosities of different types and different amounts. We cannot guess to what degree the obtained results can be applied to the general case. We cannot say the influences of viscosity in the baroclinic model are as large as in the case of our test computation. However, our analysis suggests at least that the specification of viscosity might be important in the numerical integration.

6. SUMMARIES

1. A new spherical grid system was proposed, the grid density of which is almost homogeneous. The meridional increment is constant for a given resolution. The zonal increment increases gradually from the equator to the pole by the factor of $\pi/2$. The number of grid points on the entire globe is $4N^2+2$ for the N-resolution.

2. Rules of finite-differencing on the proposed grid system were established so that the integral condition was satisfied locally at each area element.

3. The integration of the primitive equations was performed as a test of the new grid system and the finite difference schemes. The barotropic atmosphere with free surface was assumed. Starting from the same initial conditions as used by Phillips [7], the marching process was taken until the end of the 16th day with $\Delta t=10$ min. for the resolution $N=20$. In Runs 1, 2, and 3, different time integration schemes were adopted. The effect of non-linear viscosity was investigated in Runs 11, 12, 13, and 14. Test computations with linear viscosity were also made in Runs 21, 22, and 23. No noticeable distortion of the flow pattern occurred in any test run.

4. We could eliminate the (external) inertia gravitational waves of both long and short wavelengths by using the iterative integration method (Scheme B in section 4), with little effect on the prediction of the trend of the meteorological wave. The use of the iterative integration method, or at least a mixed use with other methods, seems very important for stabilizing integration. This method, however, could not suppress the development of the low-frequency short waves.

5. We could suppress the growth of short waves of both low and high frequency modes with either the non-linear or the linear viscosity. In this case, the amount of viscosity should be larger than the optimum value. By use of the optimum value, the effect of viscosity on long waves could be minimized. It is important that the optimum amount must not exceed the amount of viscosity which represents the actual diffusion process in the atmosphere.

6. So far as this numerical test was concerned, the behavior of a test run using the non-linear viscosity with a certain coefficient showed good agreement with that of a run using the linear viscosity with a certain eddy-viscosity coefficient. The analysis concerning the different effects of the different amounts of viscosity suggests a probable importance of the specification of viscosity in the numerical integration.

ACKNOWLEDGMENTS

Grateful acknowledgment is made to Dr. J. Smagorinsky for motivating the author to begin this work. He appreciates the encouraging interest and suggestions given by Drs. S. Manabe, K. Bryan, and J. Smagorinsky in this study. Prof. N. A. Phillips, Massachusetts Institute of Technology, gave him useful suggestions on the manuscript. Thanks are also due to Mr. J. L. Holloway, Jr., for reading the manuscript, Mr. E. W. Rayfield for drawing the figures, and Miss J. Neal for typing the manuscript.

REFERENCES

1. W. L. Gates and C. A. Riegel, "Comparative Numerical Integration of Simple Atmospheric Models on a Spherical Grid," *Tellus*, vol. 15, No. 4, Nov. 1963, pp. 406–423.
2. W. L. Gates and C. A. Riegel, "A Study of Numerical Errors in the Integration of Barotropic Flow on a Spherical Grid," *Journal of Geophysical Research*, vol. 67, No. 2, Feb. 1962, pp. 773–784.
3. H. L. Kuo and J. Nordö, "Integration of Four-Level Prognostic Equations over the Hemisphere," *Tellus*, vol. 11, No. 4, Nov. 1959, pp. 412–424.
4. Y. Kurihara, "On the Use of Implicit and Iterative Methods for the Time Integration of the Wave Equation," *Monthly Weather Review*, vol. 93, No. 1, Jan. 1965, pp. 33–46.
5. N. A. Phillips, "A Map Projection System Suitable for Large-Scale Numerical Weather Prediction," *Journal of the Meteorological Society of Japan*, 75 Anniversary Volume, Nov. 1957, pp. 262–267.
6. N. A. Phillips, "Numerical Integration of the Hydrostatic System of Equations with a Modified Version of the Eliassen Finite-Difference Grid," *Proceedings of the International Symposium on Numerical Weather Prediction, Tokyo, 1960*, Meteorological Society of Japan, 1962, pp. 109–120.
7. N. A. Phillips, "Numerical Integration of the Primitive Equations on the Hemisphere," *Monthly Weather Review*, vol. 87, No. 9, Sept. 1959, pp. 333–345.
8. L. F. Richardson, *Weather Prediction by Numerical Process*, Cambridge University Press, 1922, 236 pp. (p. 19 and p. 155).
9. F. G. Shuman, "Numerical Experiments with the Primitive Equations," *Proceedings of the International Symposium on Numerical Weather Prediction, Tokyo, 1960*, Meteorological Society of Japan, 1962, pp. 85–107.
10. J. Smagorinsky, "On the Numerical Integration of the Primitive Equations of Motion for Baroclinic Flow in a Closed Region," *Monthly Weather Review*, vol. 86, No. 12, Dec. 1958, pp. 457–466.

[Received February 5, 1965; revised May 4, 1965]